Separation and Purification Technology 320 (2023) 124052

Contents lists available at ScienceDirect

Separation and Purification Technology

journal homepage: www.elsevier.com/locate/seppur

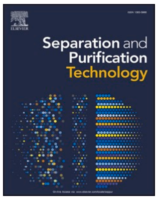

S-scheme heterojunction between MOFs and Ag_3PO_4 leads to efficient photodegradation of antibiotics in swine wastewater

Caiyu Luo [a,b], Yan Lin [a,d,*], Yupei Zhang [a], Shuai Zhang [a], Shehua Tong [a], Shaohua Wu [b], Chunping Yang [a,b,c,d,*]

[a] *College of Environmental Science and Engineering, Hunan University, Changsha, Hunan 410082, China*
[b] *Guangdong Provincial Key Laboratory of Petrochemcial Pollution Processes and Control, and Key Laboratory of Petrochemical Pollution Control of Guangdong Higher Education Institutes, School of Environmental Science and Engineering, Guangdong University of Petrochemical Technology, Maoming, Guangdong 525000, China*
[c] *School of Environmental and Chemical Engineering, Nanchang Hangkong University, Nanchang, Jiangxi 330063, China*
[d] *Hunan Province Environmental Protection Engineering Center for Organic Pollution Control of Urban Water and Wastewater, Changsha, Hunan, 410001, China*

ARTICLE INFO

Keywords:
Heterojunction
Photocatalyst
MOFs
Silver phosphate
Swine wastewater
Oxytetracycline

ABSTRACT

Antibiotics in swine wastewater could lead to risks to the environment and human health, and it is a competitive alternative to degrade antibiotics via photocatalysis which is green and eco-friendly. However, charge separation efficiency and light absorption capacity have been key factors limiting the technology. In this work, we synthesized the novel photocatalysts of MOF-545/Ag_3PO_4 via solvothermal methods, and examine the performance and mechanism for the degradation of oxytetracycline (OTC) in swine wastewater. The results showed that compared with Ag_3PO_4, the composite catalysts have stronger photoresponse and charge separation ability. MOF-545/Ag_3PO_4 could completely degrade OTC within 3.0 min with a rate constant of 3.97 min^{-1} which is 12.9 times that of Ag_3PO_4. OTC removal was still 100% within 3.0 min after 5 cycles, which confirmed that the composite catalyst was stable. Data from free radical capture tests showed that photogenerated holes (h^+) and superoxide radicals ($\bullet O_2^-$) played a dominant role in OTC degradation. In-situ X-ray photoelectron spectroscopy (XPS) spectra and electron spin resonance (ESR) spectra proved the formation of an S-scheme heterojunction in MOF-545/Ag_3PO_4, which greatly improves the carrier separation efficiency of catalysts. This study provides a novel MOF-based catalyst for improving photocatalytic performance.

1. Introduction

Tetracyclines (TCs) including oxytetracycline (OTC) are often used to promote the growth of pigs and prevent and treat diseases [1,2]. They are poorly absorbed by pigs, and the long-term use and the consequent accumulation will pose a threat to human health [3–5]. Unfortunately, these antibiotics are recalcitrant in traditional biological treatment processes for swine wastewater. Photocatalysis is a promising technique for degrading antibiotics in swine wastewater which is green and eco-friendly [6,7]. The photogenerated electron-hole pairs have a strong redox ability to degrade antibiotics [8,9]. Silver phosphate (Ag_3PO_4) photocatalyst has been widely studied because of its simple preparation method, low toxicity, and strong oxidation ability [10]. However, the limited light response range and carrier separation efficiency limits its application in practice [11–14]. To this end, a variety of methods have been employed, including particle size regulation [15], carbon material modification [16], metal deposition [17], element doping [18], and heterojunction construction [19].

The construction of heterojunction has been proven to be an effective modification method in Ag_3PO_4. For example, He et al constructed a Z-scheme heterojunction inside Ag_3PO_4/g-C_3N_4, and the CO_2 conversion of the composite was 6.1 and 10.4 times higher than that of g-C_3N_4 and P25 under simulated sunlight irradiation, respectively [20]. Cai et al fabricated an Ag_3PO_4/Ti_3C_2 Schottky catalyst, and the apparent rate constant of photodegradation of 2, 4-Dinitrophenol was 10 times that of Ag_3PO_4 [21]. Lin et al synthesized Z-scheme heterojunction photocatalysts Ag_3PO_4@MWCNTs@Cr: $SrTiO_3$, under visible light, ternary composites can completely remove malachite green in 10 min, while Ag_3PO_4 takes 30 min to degrade 99% [22].

However, traditional heterojunctions exist some inherent disadvantages, such as type-II heterojunction cannot retain the strong redox ability of single catalysts. Z-scheme heterojunction is prone to side

---

[*] Corresponding authors at: College of Environmental Science and Engineering, Hunan University, Changsha, Hunan 410082, China.
E-mail addresses: linyan@hnu.edu.cn (Y. Lin), yangc@hnu.edu.cn (C. Yang).

https://doi.org/10.1016/j.seppur.2023.124052
Received 15 March 2023; Received in revised form 5 May 2023; Accepted 6 May 2023
Available online 10 May 2023

reactions and it is difficult to achieve the expected charge transfer path. S-scheme heterojunction overcomes these shortcomings, it not only can retain the strong redox ability of single-phase catalysts but also can enhance the ability to charge transfer [23,24]. Therefore, S-scheme heterojunction was chosen to improve the photocatalytic performance of Ag_3PO_4 in this study.

The key to construct S-scheme heterojunction was to find a catalyst that is compatible with Ag_3PO_4. Metal Organic Frameworks (MOFs) have aroused great interest in pollutants treatment because of their high porosity and specific surface area, as well as the tunability and diversity of structures [25–27]. At the same time, the use of MOFs to composite with other photocatalysts has been proven to be effective to improve the light absorption capacity and the carrier separation efficiency [28,29]. Considering that the low flat band potential of Ag_3PO_4, stable zirconium-based MOF-545 with high flat band potential was selected in this work to construct S-scheme heterojunction successfully [30].

To the best of our knowledge, studies of Ag_3PO_4 with MOF-545 have not been reported. In this work, the novel photocatalysts MOF-545/Ag_3PO_4 (M/A) were successfully prepared and used to degrade OTC in swine wastewater. The morphology, light absorption capacity, carrier separation efficiency, catalytic performance and mechanism of the catalysts were discussed in detail. The results show that compared with Ag_3PO_4, the composite catalysts have stronger photoresponse and charge separation ability. MOF-545/Ag_3PO_4 could completely degrade OTC within 3.0 min with a pseudo-first-order rate constant of 3.97 min^{-1} which is 12.9 times that of Ag_3PO_4. The composite photocatalyst was stable which achieved complete removal of OTC even after five cycles. The excellent photocatalytic performance was ascribed to the S-scheme heterojunction between MOF-545 and Ag_3PO_4. This study provides a universal strategy for how to improve the light absorption capacity and charge separation efficiency of photocatalysts and a novel MOF-based catalyst for improving photocatalytic performance.

2. Material and methods

2.1. Materials

Isopropanol (IPA, $\geq$ 99.7%) was obtained from Hunan Huihong Reagent Co., Ltd. Tetrakis (4-carboxyphenyl) porphyrin (H_2TCPP, $\geq$ 97.0%) was purchased from Shanghai Haohong Biomedical Technology Co., Ltd. N, N-Diethylformamide (DEF, 99%) was done from Shanghai Yien Chemical Technology Co., Ltd. Zirconium tetrachloride ($ZrCl_4$, $\geq$ 99.9%) was obtained from Shanghai Aladdin Biochemical Technology Co., Ltd. Ethylenediaminetetraacetic acid disodium salt (EDTA-2Na, $\geq$ 99.0%), benzoquinone (BQ, $\geq$ 98.0%), N, N-Dimethylformamide (DMF, 99.5%), benzoic acid (BA, $\geq$ 99.5%), acetone ($\geq$99.5%), hydrochloric acid (36.0%~38.0%), sodium phosphate dibasic dodecahydrate ($Na_2HPO_4 \cdot 12H_2O$, $\geq$ 99.0%), silver nitrate ($AgNO_3$, $\geq$ 99.8%) were purchased from Sinopharm Chemical Reagent Co., ltd. Milli-Q water was applied throughout all experiments.

2.2. Experiments

2.2.1. Synthesis of catalysts

The synthesis method of MOF-545 has been adjusted slightly based on previous reports [31]. Typically, 0.125 g $ZrCl_4$, 0.125 g H_2TCPP, 6.75 g benzoic acid and 20 mL DEF were added to the 50 mL PTFE reactor lining. After ultrasonic dissolution, the mixture was placed in an oven at 120 °C for 48 h, followed by at 130 °C for 24 h. Then the pre-material was obtained by filtration. The next step was to activate it. The mixed solution was added to DEF (250 mL) solution containing 3.75 mL 4 M HCl and heat in an oil bath at 120 °C for 12 h. After cooling down, it was filtered and washed with acetone and DMF, then soaked in acetone for 24 h. Finally, after filtration, it was put into a 120 °C vacuum drying oven to dry for 12 h to obtain purple solid MOF-545.

3.0 mmol $Na_2HPO_4 \cdot 12H_2O$ aqueous solution was added dropwise to 9.0 mmol $AgNO_3$ aqueous solution. Then the mixture was stirred continuously in the dark for 6 h, followed by centrifugation and washing with Milli-Q water. Finally, it was dried in a vacuum drying oven at 60 °C for 12 h to obtain golden yellow solid Ag_3PO_4 particles.

The preparation flow of the MOF-545/Ag_3PO_4 was shown in Fig. S1. Specifically, x mL MOF-545 (1000 mg/L) aqueous solution was fixed to 100 mL with Milli-Q water. And then 9.0 mmol $AgNO_3$ aqueous solution was added drop-by-drop. After stirring for 6 h, 3.0 mmol $Na_2HPO_4 \cdot 12H_2O$ solution was added to it. Subsequently, the pre-solution was centrifuged and washed several times with Milli-Q water, and then dried in a 60 °C vacuum drying oven for 12 h to obtain MOF-545/Ag_3PO_4 composite photocatalysis. Written as xM/A. (x represents the number of grams of MOF-545).

2.2.2. Photodegradation experiments

OTC was added to Milli-Q water to prepare OTC wastewater with a concentration of 20 mg/L. The photoreaction system consists of 100 mL OTC solution and 50.0 mg photocatalysts. Before the photodegradation experiment began, ultrasonic dispersion was performed to make the catalysts and OTC solution mixed evenly. In order to excluded the effect of the material on the adsorption of OTC during the photoreaction, the system was stirred for 30 min under dark conditions to reach the adsorption desorption equilibrium. Subsequently, photodegradation experiments were performed. In order to prevent the solution from heating up due to light irradiation, the reaction was carried out under cooling cycle water. The light source was a xenon lamp with an intensity of 300 W and a wavelength>420 nm (PLS-SXE300/300UV, Beijing Perfectlight Technology Co.,Ltd.). During illumination, samples were taken at 0, 10, 20, 30, 40 s and 1, 3, and 5 min under light irradiation. They were filtered through 0.22 μm aqueous filter head, and then the content of OTC was detected with HPLC. The photodegradation experimental steps of tetracycline (TC) were consistent with OTC. The removal rate and corresponding reaction rate constant of TCs could be calculated by the following formulas:

$$Removalrate = 1 - C_i/C_0 \times 100\%$$

$$-ln(C_i/C_0) = kt$$

Where C_0 represents the initial concentration of the TCs before the adsorption and degradation, C_i was the concentration of TCs at a specific moment, k denotes the apparent reaction rate constant.

In order to simulate the actual situation, the swine wastewater after anaerobic treatment of a pig farm (Fuchi Farm, Hengyang, Hunan Province, N26.90°E 112.58°) was also used for photodegradation experiments. The ammonia nitrogen of it was determined to be 1800 mg/L, and the total phosphorus was 92.6 mg/L. After centrifugation to remove sediment, the water was diluted 10 times and 20 times with Milli-Q water. The content of antibiotics in the actual wastewater is slight generally, so an additional 10 mg/L OTC was added to the wastewater to make the experimental effect more obvious. The reaction system was 50.0 mg catalysts and 100 mL OTC (10.0 mg/L) swine wastewater, and other steps were consistent with the OTC degradation experiment.

2.2.3. Free radical capture experiments

In order to figure out the main active species for the degradation of OTC, free radical trapping experiments were performed. Benzoquinone (BQ), disodium ethylenediaminetetraacetate (EDTA-2Na), isopropanol (IPA), silver nitrate ($AgNO_3$) was used to scavenge superoxide radicals ($\bullet O_2^-$), photogenerated holes (h^+), hydroxyl radicals (•OH) and photogenerated electrons (e^-), respectively. The content of the trap agents was 0.01 mol/L.

2.2.4. Cycle experiments

The stability of the catalyst was determined by cycle experiments on OTC. After each photodegradation experiment, the catalytic material

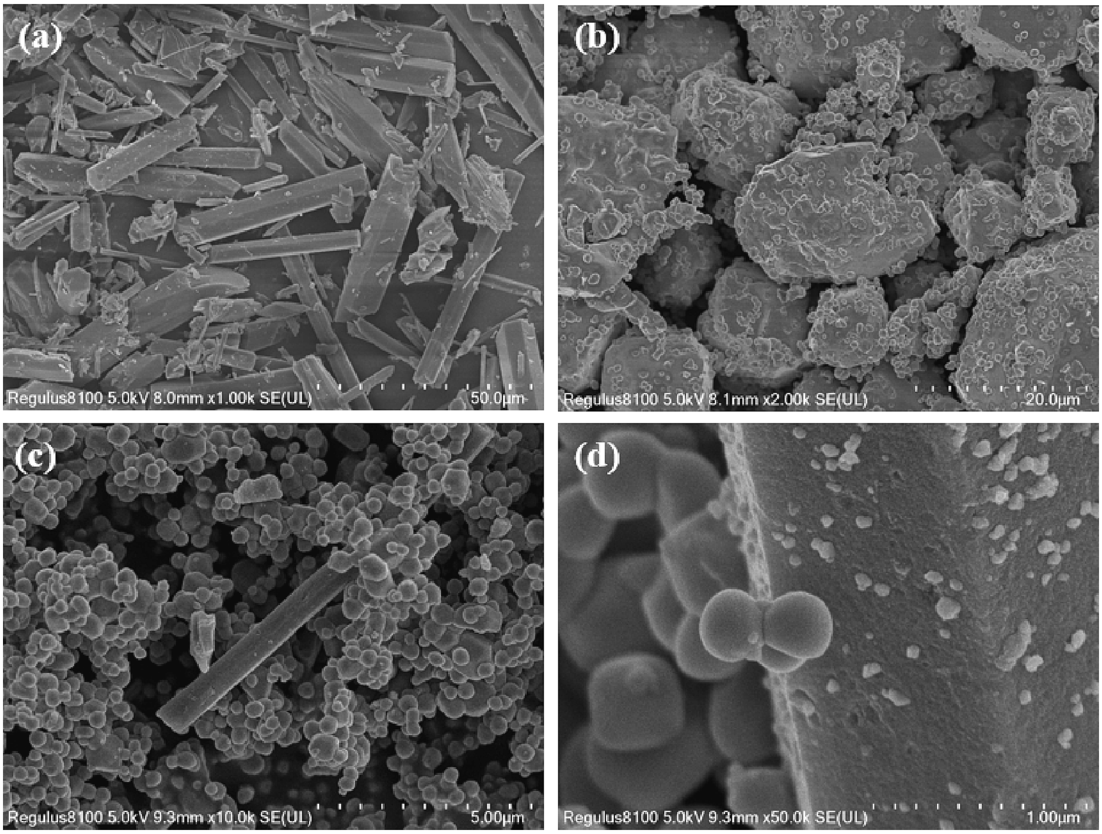

Fig. 1. SEM images of different catalysts. (a) MOF-545; (b) Ag_3PO_4; (c, d) M/A.

was filtered and washed with Milli-Q water at the same time, and then placed in a 60 °C vacuum drying chamber for 12 h, the material was used for the next cycle experiment. 5 cycles were carried out in this work.

2.2.5. *Experiments on effects of nitrogen and phosphorus*

Due to the high content of nitrogen and phosphorus in swine wastewater, the effects of nitrogen and phosphorus on the degradation of OTC in wastewater were also studied. In order to simulate the nitrogen and phosphorus content after dilution 10 times of swine wastewater. 1.29 g of dried ammonium nitrate (NH_4NO_3) was dissolved in 1000 mL OTC solution (20 mg/L), and the concentration of ammonia nitrogen in this solution is 180 mg/L; 0.0439 g KH_2PO_4 was dissolved in 1000 mL OTC solution (20 mg/L), and the content of phosphorus in this solution is 10.0 mg/L.

2.3. *Characterization*

Field emission scanning electron microscopy (FESEM, Hitachi Regulus 8100, Japan) was used to observe the surface morphology of the catalysts, and the elemental composition was determined by its supporting energy spectrometer (EDAX Octane Elect Super-70 mm2, USA). The crystal structures were characterized by X-ray diffractometer (XRD, Bruker D8 Advance, Germany). The BET specific surface of the catalysts was determined by surface area porosity analyzer (Micromeritics ASAP 2460, USA). The UV–vis diffused reflectance spectra (UV–vis DRS) were obtained by UV–vis-NIR spectrophotometer (Shimadzu UV-3600, Japan). Photoluminescence (PL) spectroscopy was studied with a full-featured steady-state/transient fluorescence spectrometer (Edinburgh Instruments, EI FLS980 Fluorescence Spectrofluorometer, UK). Electrochemical impedance spectroscopy (EIS) and Mott-Schottky plots of the prepared photocatalysts were measured by a three-electrode cell in 0.50 mol/L Na_2SO_4 aqueous solution and a CHI 760E workstation. The as-prepared photocatalysts thin-film on fluorine-doped tin oxide (FTO) was used as the working electrode. The other two electrodes were an Ag/AgCl electrode and a platinum (Pt) electrode, respectively. The surface chemical composition and electron transfer were analyzed with X-ray photoelectron spectroscopy (XPS, PHI 5000 Versaprobe III, Japan). The electron spin resonance (ESR) signals of radical spin-trapped by spin-trapped reagent 5, 5-dimethyl-L-pyrroline N-oxide (DMPO) were examined on an electron paramagnetic resonance spectrometer under visible light irradiation ($\lambda > 420$ nm) (JEOL JES FA200, Japan).

2.4. *Analytical methods*

The concentration of antibiotics was determined by high performance liquid chromatography (HPLC), the intermediate products of OTC degradation process were tested by liquid chromatograph-mass spectrometer (LC-MS), and the details are in text S1.

3. Results and discussion

3.1. *Characterization*

The morphology and microstructure of the catalysts were studied by FESEM. As shown in Fig. 1a, MOF-545 exhibited a rod-like structure with smooth surface and a certain brittleness, and the diameter was about 2–10 μm. Ag_3PO_4 were polyhedral particles with inhomogeneous particle size. The large were 10–20 μm in diameter approximately, and there were lots of small spheres of Ag_3PO_4 attached to them (Fig. 1b). However, after the addition of MOF-545, the particle size of Ag_3PO_4 became small and uniform, most of which were below 0.5 μm in diameter. This facilitated the exposure of more surface-active sites, thereby enhancing the photocatalytic efficiency of Ag_3PO_4. At the same time, MOF-545 grown through Ag_3PO_4 (Fig. 1c). In addition, there were many Ag_3PO_4 with a diameter of about 0.1 μm embedded on the surface of MOF-545 (Fig. 1d). The above phenomena indicated that great

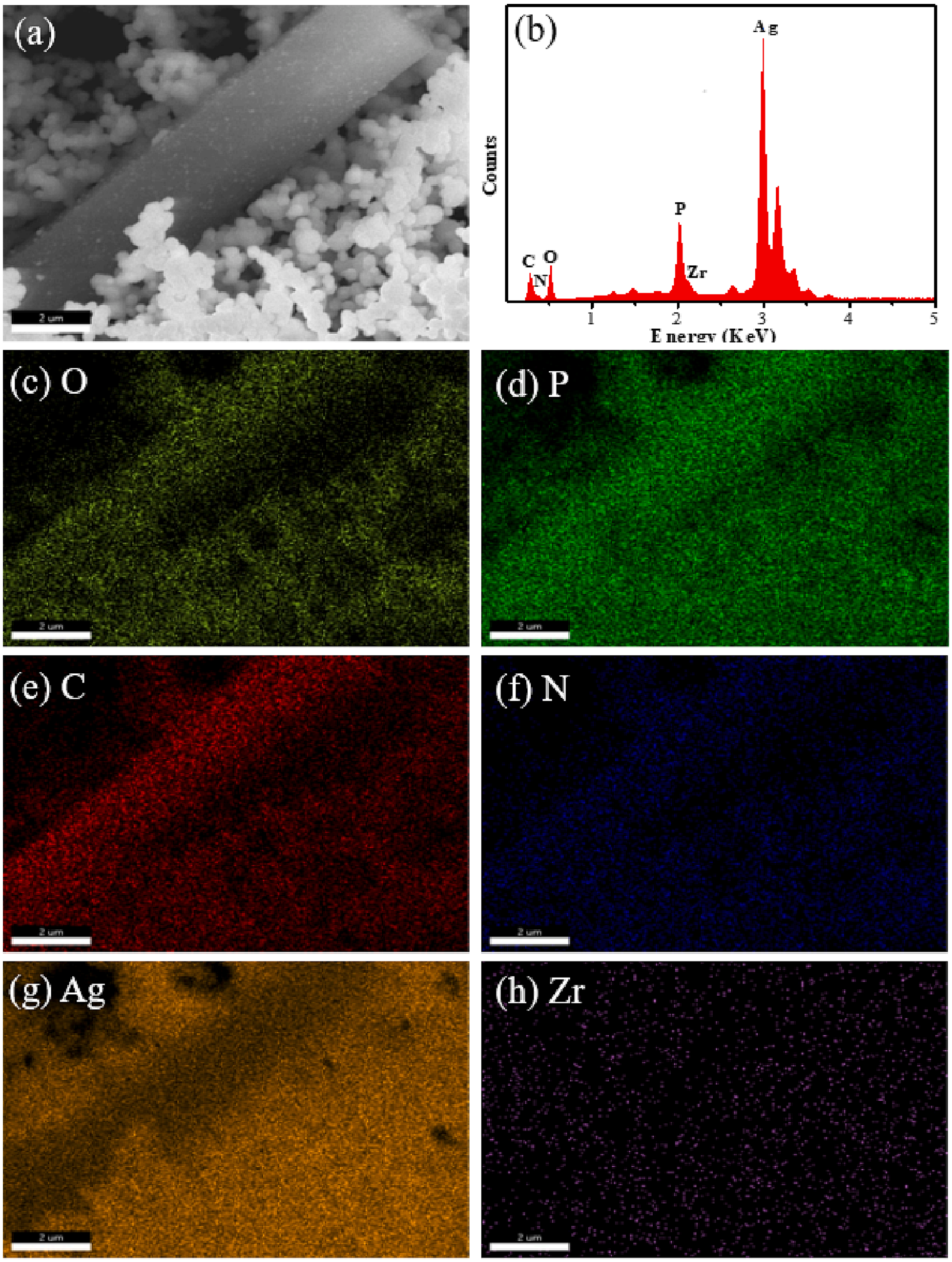

Fig. 2. SEM-EDS elemental mapping images of M/A.

interfacial contact has formed between MOF-545 and Ag_3PO_4.

In addition, the BET specific surface area of the photocatalysts was determined. In order to obtain more accurate particle size information of the catalysts, the specific surface area of BET was determined. As shown in Table S1, the BET specific surface area of Ag_3PO_4 was 0.164 $m^2 \cdot g^{-1}$ only, while the MOF-545/Ag_3PO_4 reached 3.79 $m^2 \cdot g^{-1}$ which is 23.1 times that of Ag_3PO_4. Generally, a larger surface area will make more active species and pollutant molecules adsorb on the surface of the photocatalyst, thus improving the photocatalytic activity of the catalyst [32,33]. In addition, SEM-EDS tests were also carried out and the results was shown in Fig. 2. The elements P, Ag, O, C, N, H, and Zr could all be observed, proving that Ag_3PO_4 grew well on the surface of MOF-545. To study the crystal structure of the material, XRD tests were performed. As shown in Fig. S2, the prepared Ag_3PO_4 was anastomosed with the Ag_3PO_4 of the body-centered cubic crystal form (JCPDS No.06-0505), the main diffraction peaks at 20.9°, 29.7°, 33.3°, 36.6°, 53.4°, 55.0°, 57.3° and 71.9°, were indexed as the (110), (200), (210), (211), (222), (320), (321) and (421) crystal planes, respectively. [34]. The XRD profile of MOF-545 was consistent with previous studies [35]. In the XRD pattern of the composite catalyst, the characteristic peaks of Ag_3PO_4 and MOF-545 could be clearly observed. The above conclusions indicated the successful synthesis of Ag_3PO_4, MOF-545 and MOF-545/Ag_3PO_4.

High resolution XPS was used to determine the chemical composition of the catalyst surface. Fig. 3a showed the spectrum of N 1s of MOF-545, with peaks at 400.01 eV and 397.80 eV corresponding to pyrrole N and C = C-N, respectively. The Zr 3d spectrum corresponded to two peaks, 185.30 eV and 182.80 eV, which related to Zr $3d_{3/2}$ and Zr $3d_{5/2}$, respectively (Fig. 3b). Fig. 3c could be observed that C 1s of MOF-545 included three characteristic peaks located at 284.80 eV, 286.36 eV and 288.83 eV, which were derived from the C = C bond and amorphous carbon of the aromatic ring, the carbon–nitrogen bond, carboxylic acid

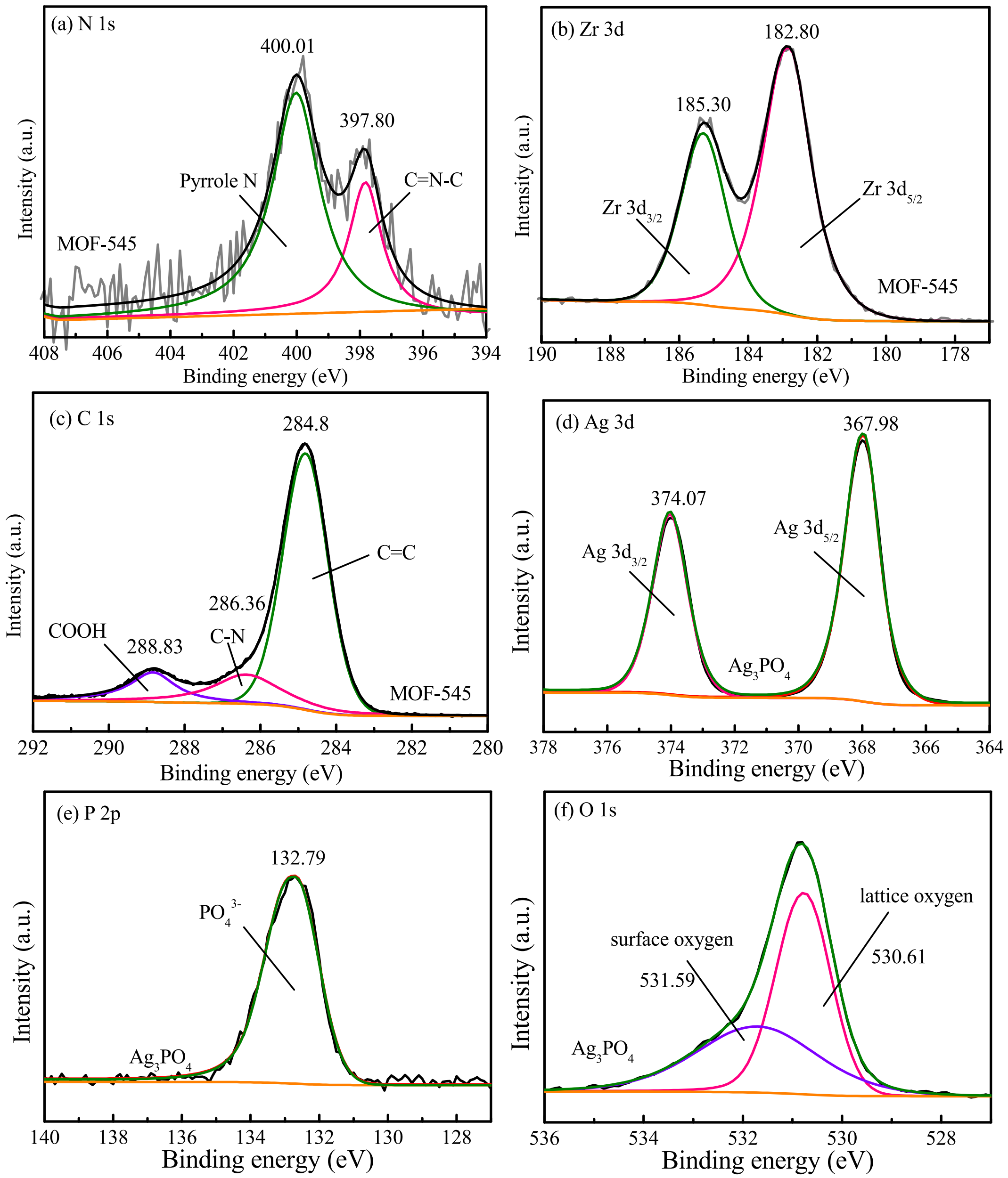

Fig. 3. High resolution XPS spectrum. (a) N 1s spectra of MOF-545; (b) Zr 3d spectra of MOF-545; (c) C 1s spectra of MOF-545; (d) Ag 3d spectra of Ag_3PO_4; (e) P 2p spectra of Ag_3PO_4; (f) O 1s spectra of Ag_3PO_4.

and the carboxyl group of the pyrrole ring, respectively [36]. For Ag_3PO_4, Ag 3d had two characteristic peaks, 367.98 eV and 374.07 eV, corresponding to Ag $3d_{5/2}$ and $3d_{3/2}$, respectively, which indicated the presence of Ag^+ in Ag_3PO_4 (Fig. 3d) [37]. The characteristic peak of P 2p was located at 132.79 eV, which was mainly due to the presence of PO_4^{3-} in Ag_3PO_4 (Fig. 3e) [37]. The O1s spectrum was divided into two distinct peaks, 530.5 eV and 531.9 eV, corresponding to lattice oxygen and surface oxygen of Ag_3PO_4, respectively (Fig. 3f) [38].

The optical absorption capacity of the photocatalyst was tested by UV–vis diffuse reflectance spectrum (DRS) and the band gap of the materials was calculated. As shown in Fig. 4a, the pure Ag_3PO_4 has good capture absorption performance at wavelengths less than 530 nm, but weak above 530 nm. After compounding with MOF-545, the absorption intensity is greatly enhanced, even above 530 nm. The reason is that MOF-545 contains an H_2TCPP ligand, which acts as a visible light capture unit, thereby improving the optical absorption performance of the catalyst [31]. The Tauc plot of Ag_3PO_4 was shown in Fig. 4b, and it is clear that the band gap of Ag_3PO_4 is 2.34 eV. The UV–vis DRS of MOF-545 was shown in Fig. S3a, which has a strong light absorption ability below 700 nm. Similarly, the band gap of MOF-545 is calculated to be 1.60 eV (Fig. S3b).

In order to study the band structure of photocatalysts, the Mott–-Schottky curves of Ag_3PO_4 and MOF-545 were tested under the frequency of 750 Hz and 1000 Hz, respectively. As shown in Fig. 4c, d, the slope of both straight segments is positive, proving that Ag_3PO_4 and MOF-545 are both n-type semiconductors. Fig. 4c manifested that the E_{fb} of Ag_3PO_4 is 0.365 eV vs. Ag/AgCl, which is equivalent to 0.562 eV vs. NHE. Since the E_{CB} of n-type semiconductors is 0.2 V higher than that of E_{fb}, the E_{CB} of Ag_3PO_4 is 0.36 eV [39]. Thus, the E_{VB} of Ag_3PO_4 is 2.70 eV. Similarly, the E_{CB} and E_{VB} of MOF-545 are −0.39 eV and 1.21 eV. The above calculated values are similar to the previous results [31,40].

To study the separation efficiency of the carriers, the photoluminescence (PL) spectrums of the catalysts at an excitation wavelength of 320 nm were tested. As shown in Fig. 5a, the PL strength of

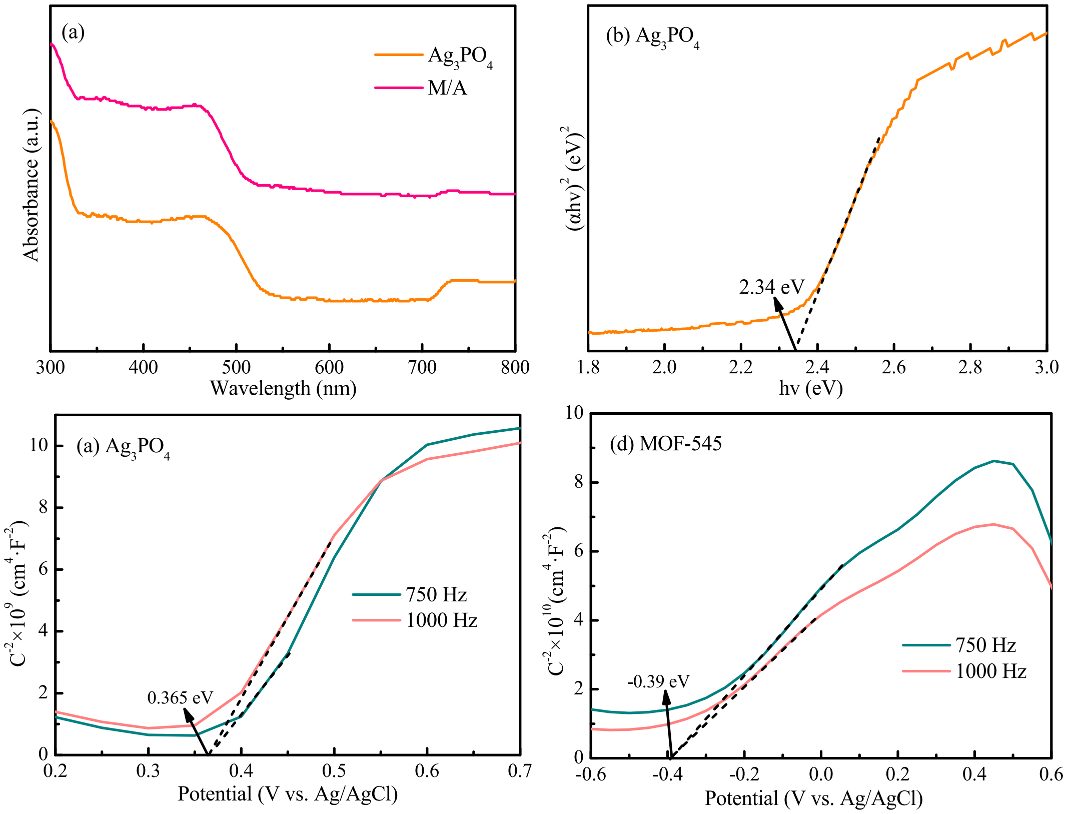

Fig. 4. Spectrum of catalysts. (a) UV Vis DRS spectrum of Ag_3PO_4 and M/A; (b) Tauc plot of Ag_3PO_4; (c) Mott–Schottky plot of Ag_3PO_4; (d) Mott–Schottky plot of MOF-545.

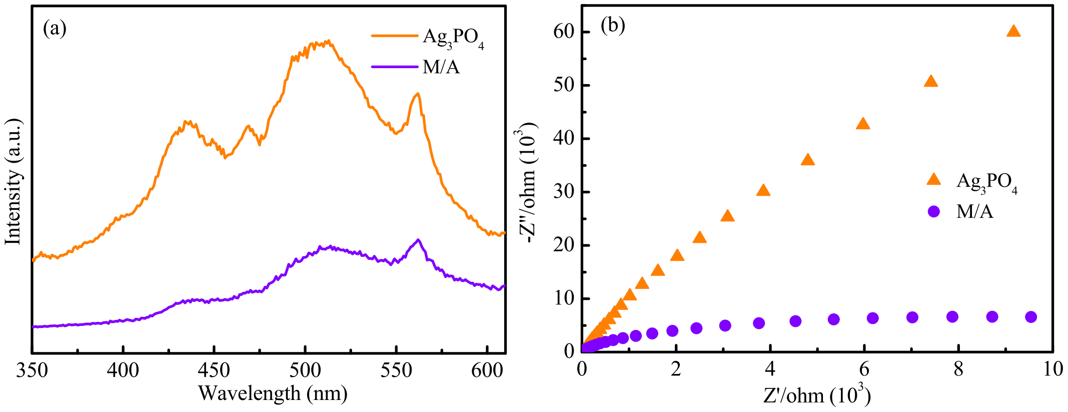

Fig. 5. Spectrum of Ag_3PO_4 and M/A. (a) PL spectra; (b) EIS plot.

Ag_3PO_4 is significantly stronger than that of MOF-545/Ag_3PO_4, which indicates that the doping of MOF-545 improves the separation efficiency of photogenerated carriers [41,42]. In addition, electrochemical impedance spectroscopy (EIS) tests were performed on the materials. The reduced radius of the impedance spectrum means that photogenerated electron-hole pairs have higher migration and separation efficiency [43,44]. As shown in Fig. 5b, the radius of the MOF-545/Ag_3PO_4 is smaller than that of Ag_3PO_4, indicating that the electron transfer ability of the MOF-545/Ag_3PO_4 composite is stronger. The above conclusions showed that the introduction of MOF-545 significantly improved the photogenerated charge separation efficiency of the Ag_3PO_4, generated more effective photogenerated carriers, and greatly improved the photocatalytic ability.

3.2. Photocatalytic performance

3.2.1. Photodegradation activity of catalysts on OTC and TC

The degradation of OTC was used to evaluate the performance of the photocatalysts. Fig. 6a presented the adsorption equilibrium curve for OTC of Ag_3PO_4 and MOF-545/Ag_3PO_4 within 60 min, it could be found that the adsorption capacity of OTC by photocatalytic materials was slight, and the adsorption–desorption equilibrium had been reached at 30 min, which indicated that the degradation of OTC under light was all attributed to photoreaction, and the influence of adsorption was excluded.

The degradation curve of OTC by photocatalysts was shown in Fig. 6b. The photocatalytic activity of all MOF-545/Ag_3PO_4 was superior to the Ag_3PO_4, and they could completely remove OTC in 3 min. However, the degradation rate of Ag_3PO_4 in 3 min was only about 65%, and it

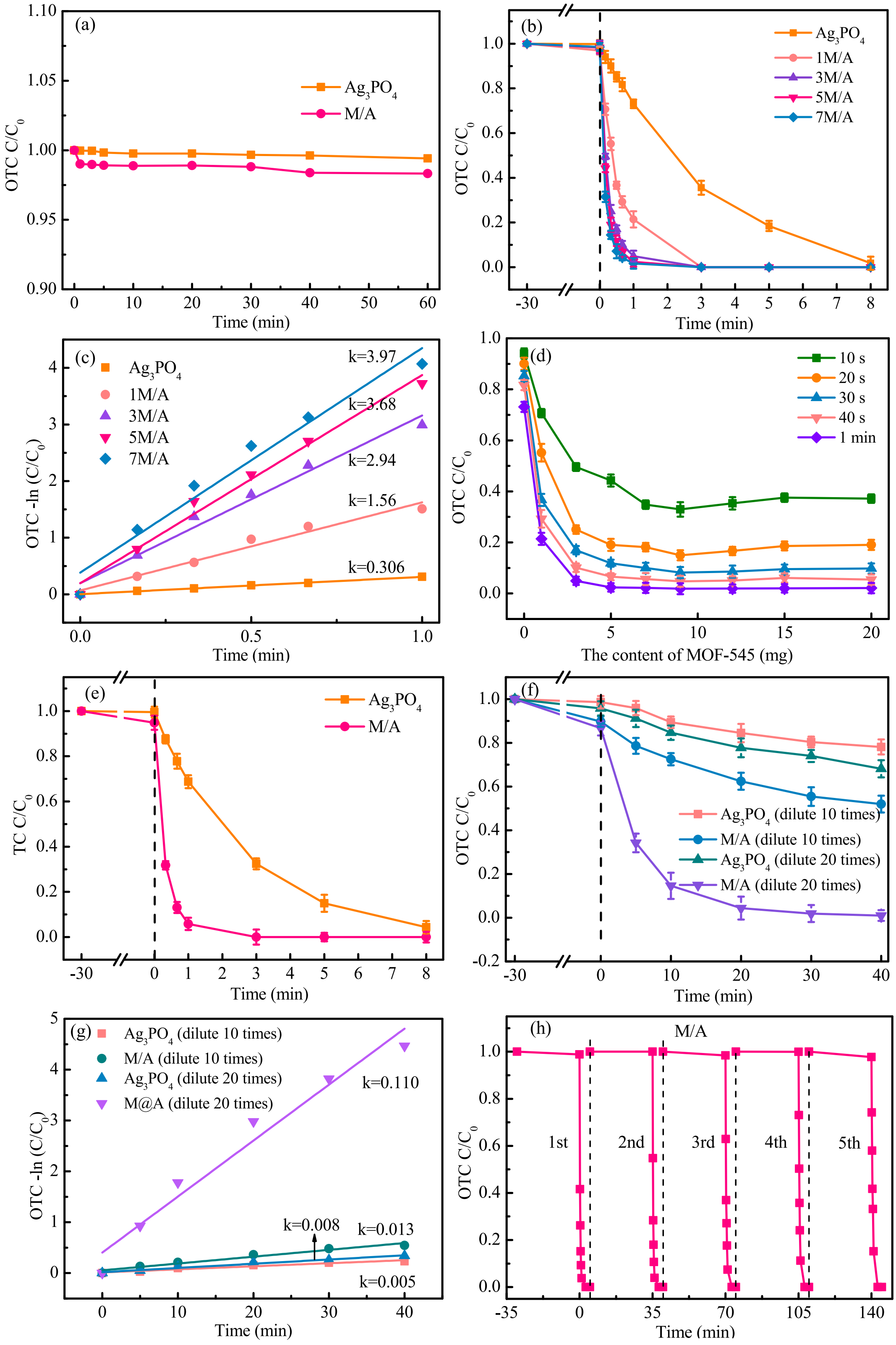

Fig. 6. Photodegradation curves of Ag_3PO_4 and M/A. (a) adsorption–desorption equilibrium curves of Ag_3PO_4 and MOF-545; (b) degradation curve of OTC by M/A with different MOF-545 content, (c) corresponding reaction kinetics curve; (d) degradation curve of OTC as the MOF-545 content changed; (e) degradation curve of TC; (f) degradation curves of swine wastewater with different dilution times; (g) corresponding reaction kinetics curve; (h) cycling experiments for the photocatalytic degradation of OTC by M/A.

Table 1
Comparison with other photocatalysts for degradation.

Photocatalyst	Dosage (g/L)	OTC concentration (mg/L)	Light source	Irradiation time (min)	Remove rate (%)	Refs.
Co-pCN	0.3	20	300 W Xe lamp (λ ≥ 420 nm)	40	75.7	[45]
CoFe@NSC	0.2	50	300 W Xe lamp (λ ≥ 400 nm)	150	82.7%	[46]
$Fe_{2.8}Ce_{0.2}O_4$/GO	0.8	30	220 W Xe lamp (λ > 420 nm)	120	88%	[47]
OCN-24-550	1	20	300 W Xe lamp (λ ≥ 420 nm)	120	85.76%	[48]
FeOOH QDs/CQDs/g-C_3N_4	0.25	10	300 W Xe lamp (λ ≥ 420 nm)	60	85.5%	[49]
BiOBr/MoS_2/GO	1	20	300 W Xe lamp (λ ≥ 380 nm)	40	98%	[50]
$MnFe_2O_4$/g-C_3N_4	0.25	30	300 W Xe lamp	10	80.5%	[51]
Ag/$BiVO_4$/GO	0.4	20	500 W Xe lamp (λ ≥ 420 nm)	70	90.43%	[52]
Ag_3PO_4	0.2	20	300 W Xe lamp (λ ≥ 420 nm)	8	98.2%	This work
MOF-545/Ag_3PO_4	0.2	20	300 W Xe lamp (λ ≥ 420 nm)	3	100%	This work

could not degrade OTC completely even in 8 min. In addition, the pseudo-first-order kinetic model was used to analyze the degradation experimental data. As shown in Fig. 6c, the K value of pure Ag_3PO_4 was 0.306 min^{-1}, and the K value of all composites was larger than that of Ag_3PO_4, among which 7 M/A reached 3.97 min^{-1}. The photocatalytic activity was increased by 12.9 times. The influence of the doping content of MOF-545 on the degradation efficiency was further studied. As shown in Fig. 6d, with the increase of MOF-545 content, the photocatalytic activity gradually increased, and the catalytic performance of the catalyst tended to be balanced after 7 mg. The reason may be the combination of MOF to Ag_3PO_4 has reached saturation, and excess MOF-545 will be washed out by Milli-Q water during synthesis. In addition, the degradation effect of the catalysts on TC was also carried out, and it is obvious that the performance of the MOF-545/Ag_3PO_4 was also significantly higher than that of Ag_3PO_4 (Fig. 6e). The above results showed that MOF-545/Ag_3PO_4 has excellent photocatalytic performance. This is attributed to the increase in the specific surface area of BET, the enhancement of light absorption capacity, and the improvement of charge separation efficiency.

3.2.2. Photodegradation activity of catalysts on OTC in simulated swine water

In order to better evaluate the ability of catalysts to remove antibiotics from swine wastewater, the swine wastewater after anaerobic treatment of a pig farm (Fuchi Farm, Hengyang, Hunan Province, N26.90°E 112.58°) was also used for photodegradation experiments. As shown in Fig. 6f. Obviously, whether it was diluted 10 times or 20 times, the degradation efficiency of MOF-545/Ag_3PO_4 was better than that of pure Ag_3PO_4. When diluted 20 times, the difference between the two catalysts was more evident. This is because many substances in high-concentration wastewater that affect the efficiency of the catalysts such as nitrogen and phosphorus etc. In addition, pseudo-first-order rate constants were used to fit the experimental data. When diluted 10 times, the k-value of MOF-545/Ag_3PO_4 was 2.6 times that of Ag_3PO_4, and when diluted 20 times, it was 13.8 times (Fig. 6g).

3.2.3. The stability of MOF-545/Ag_3PO_4 and the effect of nitrogen and phosphorus on the MOF-545/Ag_3PO_4

The result of the cycling experiment was shown in Fig. 6h, the photoactivity of MOF-545/Ag_3PO_4 was slightly reduced after five cycles, but the OTC could still be completely removed within 3 min, indicating that the materials exist great stability. In summary, MOF-545/Ag_3PO_4 has the possibility of practical application. The effects of ammonia nitrogen and total phosphorus on the degradation efficiency of OTC were shown in Fig. S4, it can be seen that ammonia nitrogen and total phosphorus inhibited the activity of the catalyst. Therefore, removing OTC in swine water by photocatalysts is suitable after nitrogen and phosphorus removal. Meanwhile, the degradation activity of MOF-545/

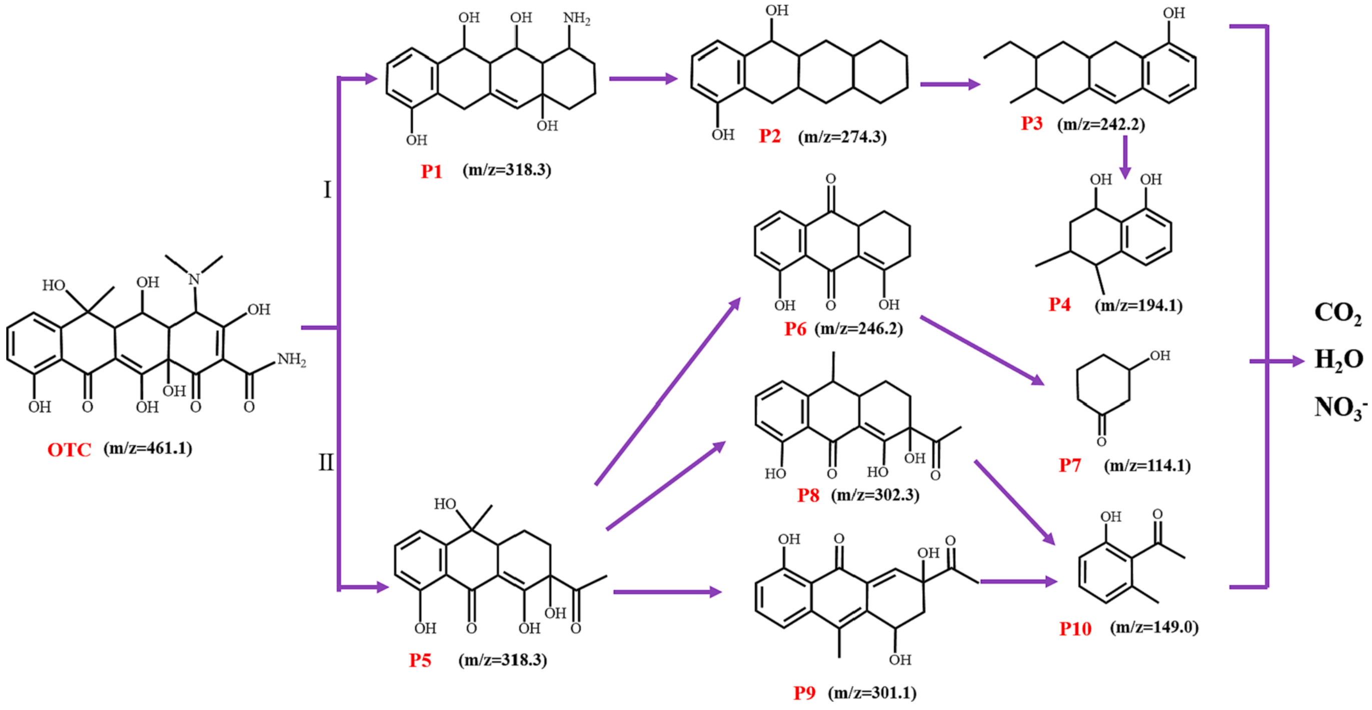

Fig. 7. Proposed degradation pathways of OTC by M/A.

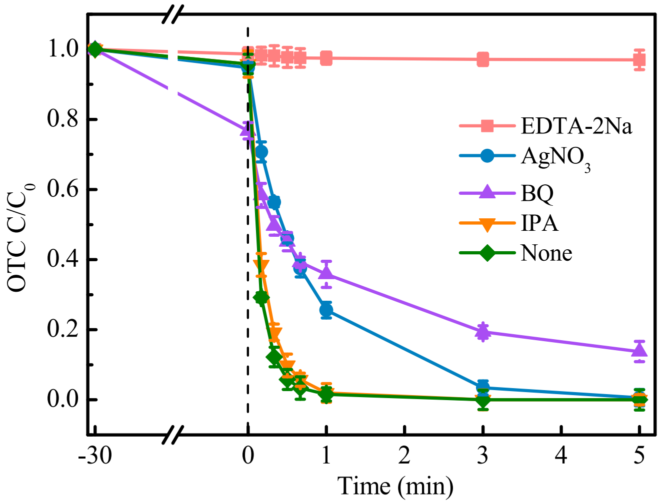

Fig. 8. Photodegradation curves of OTC over M/A composite with different active species scavengers under visible light irradiation.

Ag_3PO_4 on OTC is higher than most other photocatalysts reported previously (Table 1).

3.3. Degradation pathways of OTC

LC-MS was used to determine the intermediate degradation products of OTC by MOF-545/Ag_3PO_4, and the degradation pathway was also analyzed. The peak at $m/z = 461.1$ wasn't detected in the samples that had been reacted under light for 3 min, indicating that OTC had been completely decomposed. In addition, 10 intermediates were detected. Table S2 summarized the retention times, major mass fragment ions (m/z), chemical formulas, and possible chemical structures of these intermediates. MS spectra of the intermediate products at different reaction times were shown in Fig. S5. By analysis, there may be two pathways for the degradation of OTC. As shown in Fig. 7, in pathway I, the amino, hydroxyl, methyl, and carbonyl groups on OTC molecules could be removed to form P1. P1 removed two hydroxyl groups and one amino group, resulting in the formation of P2. P2 removed a hydroxyl group and generated P3 by ring-opening reaction, followed by hydroxylation and ring breaking to form P4 [53]. In pathway II, OTC was converted to P5 by separation of hydroxyl, dimethylamino, amide groups and ring-opening reaction. P5 was deacetylated and then the hydroxyl group was replaced by the ketone group to form P6, which was further converted to P7 [54,55]. P5 could also be dehydroxylified to produce P8 or P9, and then underwent a series of dissociative functional groups and ring-opening reactions to form P10 [56]. Finally, small molecule organic matter was mineralized into CO_2, H_2O and NO_3^- [54].

3.4. Photocatalytic mechanisms

The results of the free radical capture experiment were shown in Fig. 8. After the addition of EDTA-2Na, OTC was almost non-degraded, which indicated that photogenerated holes played a crucial role in this reaction system, mainly because of the deep valence band of Ag_3PO_4. At the same time, it was observed that the presence of BQ also had a great negative impact on the degradation of OTC, indicating that $\bullet O_2^-$ was another major active substance in the photodegradation process. After adding $AgNO_3$, the degradation efficiency of the catalyst was also reduced, indicating that photogenerated electrons also played a role. However, the presence of IPA had a limited inhibitory effect on OTC

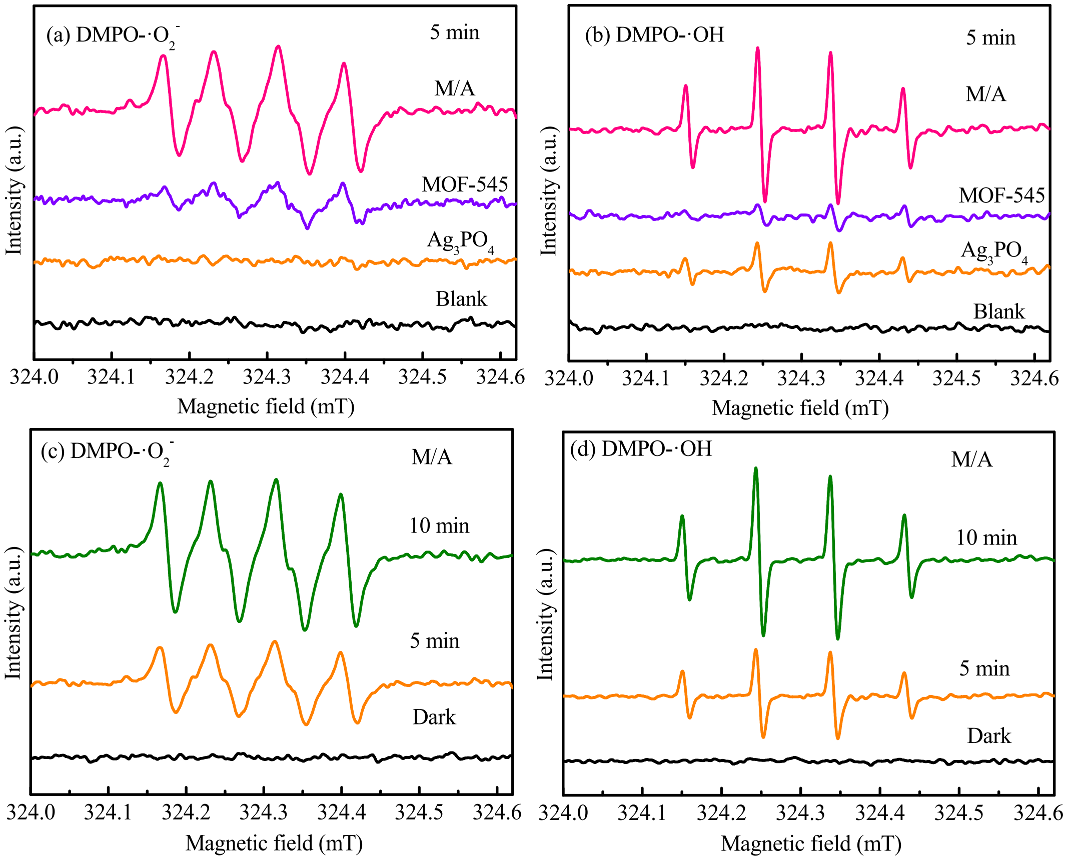

Fig. 9. ESR spectra of radical adducts trapped by DMPO in the dispersion of the different samples under both the dark and visible light irradiation (λ > 420 nm) condition. (a, c) DMPO-$\bullet O_2^-$, (b, d) DMPO-•OH.

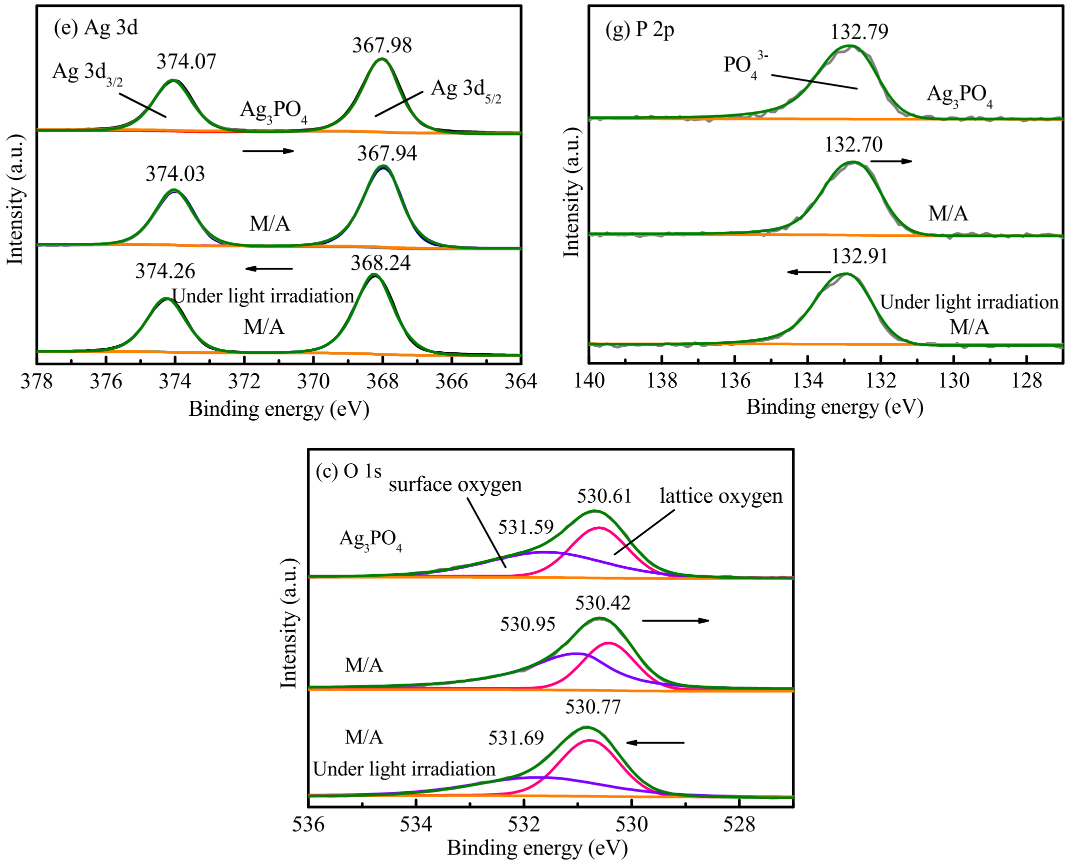

Fig. 10. In-situ XPS spectra. (a) Ag 3d samples tested in darkness and under illumination (λ > 420 nm); (b) P 2p samples tested in darkness and under illumination (λ > 420 nm); (c) O 1s spectra of pure Ag_3PO_4 and M/A samples tested in darkness and under illumination (λ > 420 nm).

degradation, indicating that the role of •OH in the reaction was slight. The above results show that photogenerated holes and superoxide radicals play a major role in the degradation of OTC.

In order to further study the reactive radicals generated by photocatalysts, ESR spectra of radical adducts trapped by DMPO in the dispersion of different samples were performed under both the dark and visible light irradiation (λ > 420 nm) condition. As shown in Fig. 9a, MOF-545 could only produce trace amounts of $\bullet O_2^-$ under light irradiation mainly because the single-catalyst carrier recombination rate is too fast. $\bullet O_2^-$ could not be detected in Ag_3PO_4, this is because the reduction potential of $O_2/\bullet O_2^-$ (-0.33 eV) is more negative than the E_{CB} of Ag_3PO_4 (+0.36 eV) [22]. The signal of $\bullet O_2^-$ in the composite MOF-545/Ag_3PO_4 was significantly enhanced, indicating that the carrier separation efficiency had been improved. Similarly, in Fig. 9b, the Ag_3PO_4 produced only slight •OH due to a more positive E_{VB} (+2.70 eV) compared with the OH/•OH potentials (+2.40 eV). While the signal

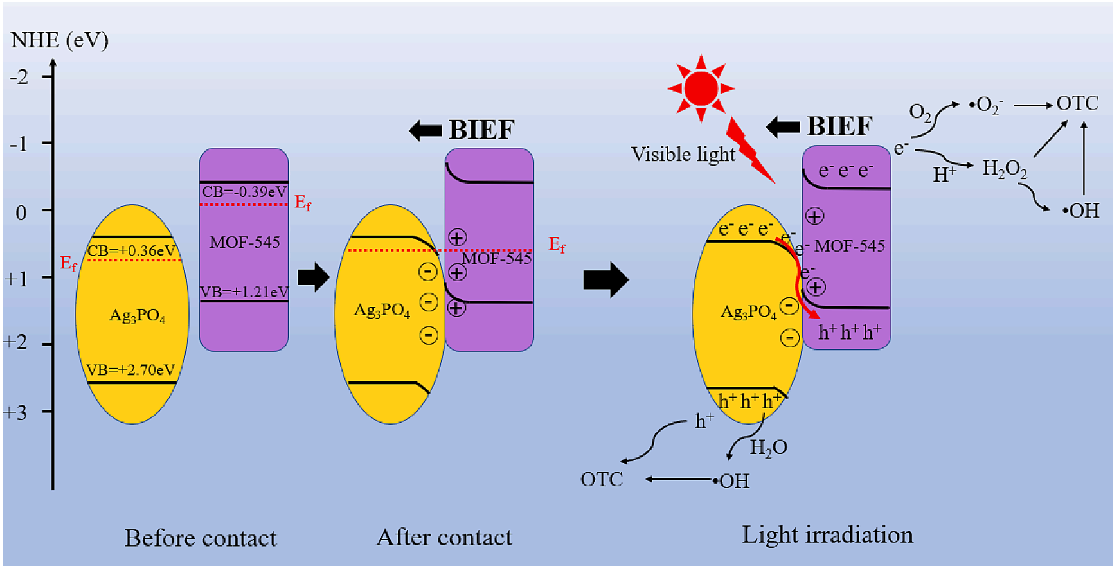

Fig. 11. Schematic illustration of photocatalytic mechanism for M/A composite under visible light irradiation (BIEF refers to built-in electric field).

intensity of •OH in MOF-545/Ag_3PO_4 was significantly enhanced, which is consistent with the conclusions obtained by $\bullet O_2^-$. In addition, for composite MOF-545/Ag_3PO_4, ESR detection was performed under dark conditions, 5 min and 10 min of illumination. As can be seen in Fig. 9c, d, the peak of $\bullet O_2^-$ and •OH were not detected in the dark, but were detected strongly under visible light conditions, and the intensity of the peaks was higher as the light time increased. The above ESR test results show that under visible light irradiation, MOF-545/Ag_3PO_4 composite photocatalyst can be successfully generated $\bullet O_2^-$ and •OH radicals, which coincided with the results of free radical capture experiments. At the same time, it also shows that the composite material has excellent carrier separation ability.

In addition, ESR proved that the heterojunction inside MOF-545 and Ag_3PO_4 was not a type-II heterojunction, but S-scheme heterojunction. Because in the case of a type-II heterojunction, the photogenerated holes on the VB of Ag_3PO_4 are transferred to MOF-545, and the photogenerated electrons on the CB of MOF-545 are transferred to the Ag_3PO_4. However, the CB of the Ag_3PO_4 and the VB of MOF-545 do not have the ability to generate $\bullet O_2^-$ and •OH [57].

In-situ XPS was used to determine the electron transfer at the interface and further demonstrate that S-scheme heterojunction exists between MOF-545 and Ag_3PO_4. As shown in Fig. 10a, when the Ag_3PO_4 was compounded with MOF-545, the binding energy of Ag $3d_{3/2}$ reduced from 374.07 eV to 374.03 eV, indicating that the Ag_3PO_4 obtained electrons in this process. This is because the Fermi level is approximately equal to the flat band potential measured by the Mott--Schottky test [58], which means that the Fermi level of MOF-545 is higher than that of the Ag_3PO_4. When the two came into contact, the electrons on the MOF-545 were transferred to the Ag_3PO_4, which created a built-in electric field (BIEF) at MOF-545/ Ag_3PO_4 interfaces pointing from MOF-545 to Ag_3PO_4 and bent the energy bands of MOF-545 and Ag_3PO_4 (Fig. 11) [59,60]. When irradiated under visible light, the binding energy of Ag $3d_{3/2}$ was significantly increased from 374.03 eV to 374.26 eV. The reason is that under the drive of the built-in electric field and band bending, the electrons generated at the conduction band of Ag_3PO_4 were transferred to the valence band of MOF-545, and connected to the photogenerated hole here (Fig. 11) [61]. Similarly, the binding energy of P 2p and O 1s decreased after contact with MOF-545 and increased under illumination, which is consistent with Ag 3d (Fig. 10b, c). The above conclusions showed that the S-scheme heterojunction between MOF-545 and Ag_3PO_4 interfaces has been successfully constructed. This greatly improved the separation efficiency of photogenerated electron-hole pairs, thereby improving the photocatalytic performance of the catalyst.

4. Conclusions

In this work, the novel photocatalysts MOF-545/Ag_3PO_4 were successfully synthesized, which achieved a stronger photoresponse and charge separation ability compared with Ag_3PO_4. The experimental results showed that the photocatalyst could completely degrade OTC in 3.0 min at a rate constant of 3.97 min^{-1} which is 12.9 times that of Ag_3PO_4. The composite catalyst was stable which achieved complete removal of OTC even after five cycles. For the degradation of OTC in simulated swine wastewater, the degradation efficiency of MOF-545/Ag_3PO_4 was also higher than that of Ag_3PO_4, indicating that the catalyst has the potential for practical utilization. S-scheme heterojunction was confirmed which contributed heavily to the excellent photocatalytic performance. This study provides a promising MOF-based photocatalyst for the removal of antibiotics from swine wastewater, and provides a strategy for how to improve the light absorption capacity and charge separation efficiency of photocatalysts.

CRediT authorship contribution statement

Caiyu Luo: Conceptualization, Methodology, Investigation, Writing – original draft, Writing – review & editing. **Yan Lin:** Conceptualization, Funding acquisition, Writing – original draft, Writing – review & editing. **Yupei Zhang:** Data curation, Investigation, Writing – original draft. **Shuai Zhang:** Formal analysis, Validation, Writing – original draft. **Shehua Tong:** Data curation, Writing – original draft. **Shaohua Wu:** Validation, Writing – original draft. **Chunping Yang:** Conceptualization, Supervision, Resources, Project administration, Funding acquisition, Writing – original draft, Writing – review & editing.

Declaration of Competing Interest

The authors declare that they have no known competing financial interests or personal relationships that could have appeared to influence the work reported in this paper.

Data availability

Data will be made available on request.

Acknowledgments

This work was funded by the National Natural Science Foundation of China (Grant Nos.: 52200093, 52270064, 51978178, and 51521006), the Department of Science and Technology of Guangdong Province of China (Contract No.: 2019A1515012044), Key Laboratory of Petrochemical Pollution Control of Guangdong Higher Education Institutes (KLGHEI 2017KSYS004), the Science and Technology Innovation Program of Hunan Province of China (Contract No.: 2021RC2058), China Postdoctoral Science Foundation (No.: 2021M701150), Hunan Provincial Natural Science Foundation of China (Contract No.: 2022JJ40036), Changsha Municipal Natural Science Foundation (Contract No.: kq2202167), and the Startup Fund of Guangdong University of Petrochemical Technology (Contract No.: 2018rc63).

Appendix A. Supplementary material

Supplementary data to this article can be found online at https://doi.org/10.1016/j.seppur.2023.124052.

References

[1] D. Cheng, H.H. Ngo, W. Guo, S.W. Chang, D.D. Nguyen, Y. Liu, X. Shan, L. D. Nghiem, L.N. Nguyen, Removal process of antibiotics during anaerobic treatment of swine wastewater, Bioresour. Technol. 300 (2020), 122707, https://doi.org/10.1016/j.biortech.2019.122707.

[2] L. Xu, H. Zhang, P. Xiong, Q. Zhu, C. Liao, G. Jiang, Occurrence, fate, and risk assessment of typical tetracycline antibiotics in the aquatic environment: a review, Sci. Total Environ. 753 (2021), 141975, https://doi.org/10.1016/j.scitotenv.2020.141975.

[3] D.L. Cheng, H.H. Ngo, W.S. Guo, Y.W. Liu, J.L. Zhou, S.W. Chang, D.D. Nguyen, X. T. Bui, X.B. Zhang, Bioprocessing for elimination antibiotics and hormones from swine wastewater, Sci. Total Environ. 621 (2018) 1664–1682, https://doi.org/10.1016/j.scitotenv.2017.10.059.

[4] B.L. Phoon, C.C. Ong, M.S. Mohamed Saheed, P.L. Show, J.S. Chang, T.C. Ling, S. S. Lam, J.C. Juan, Conventional and emerging technologies for removal of antibiotics from wastewater, J. Hazardous Mater. 400 (2020), 122961, https://doi.org/10.1016/j.jhazmat.2020.122961.

[5] Y. He, Q. Yuan, J. Mathieu, L. Stadler, N. Senehi, R. Sun, P.J.J. Alvarez, Antibiotic resistance genes from livestock waste: occurrence, dissemination, and treatment, npj Clean Water 3 (1) (2020), https://doi.org/10.1038/s41545-020-0051-0.

[6] M. Sayed, B. Ren, A.M. Ali, A. Al-Anazi, M.N. Nadagouda, A.A. Ismail, D. D. Dionysiou, Solar light induced photocatalytic activation of peroxymonosulfate by ultra-thin Ti^{3+} self-doped Fe_2O_3/TiO_2 nanoflakes for the degradation of naphthalene, Appl. Catal. B 315 (2022), 121532, https://doi.org/10.1016/j.apcatb.2022.121532.

[7] Y. Ye, J. Jin, F. Chen, D.D. Dionysiou, Y. Feng, B. Liang, H.-Y. Cheng, Z. Qin, X. Tang, H. Li, D. Yntema, C. Li, Y. Chen, Y. Wang, Removal and recovery of aqueous U(VI) by heterogeneous photocatalysis: progress and challenges, Chem. Eng. J. 450 (2022), 138317, https://doi.org/10.1016/j.cej.2022.138317.

[8] C. Bie, H. Yu, B. Cheng, W. Ho, J. Fan, J. Yu, Design, fabrication, and mechanism of nitrogen-doped graphene-based photocatalyst, Adv. Mater. 33 (9) (2021), e2003521, https://doi.org/10.1002/adma.202003521.

[9] D. Li, J. Huang, R. Li, P. Chen, D. Chen, M. Cai, H. Liu, Y. Feng, W. Lv, G. Liu, Synthesis of a carbon dots modified g-C_3N_4/SnO_2 Z-scheme photocatalyst with superior photocatalytic activity for PPCPs degradation under visible light irradiation, J. Hazard. Mater. 401 (2021), 123257, https://doi.org/10.1016/j.jhazmat.2020.123257.

[10] D.J. Martin, G. Liu, S.J. Moniz, Y. Bi, A.M. Beale, J. Ye, J. Tang, Efficient visible driven photocatalyst, silver phosphate: performance, understanding and perspective, Chem. Soc. Rev. 44 (21) (2015) 7808–7828, https://doi.org/10.1039/c5cs00380f.

[11] A. Kumar, P. Choudhary, A. Kumar, P.H.C. Camargo, V. Krishnan, Recent advances in plasmonic photocatalysis based on TiO_2 and noble metal nanoparticles for energy conversion, environmental remediation, and organic synthesis, Small 18 (1) (2022), e2101638, https://doi.org/10.1002/smll.202101638.

[12] S. Wang, J. Wang, Magnetic 2D/2D oxygen doped g-C_3N_4/biochar composite to activate peroxymonosulfate for degradation of emerging organic pollutants, J. Hazard. Mater. 423 (2022), 127207, https://doi.org/10.1016/j.jhazmat.2021.127207.

[13] Y. Lin, X. Wu, Y. Han, C. Yang, Y. Ma, C. Du, Q. Teng, H. Liu, Y. Zhong, Spatial separation of photogenerated carriers and enhanced photocatalytic performance on Ag_3PO_4 catalysts via coupling with PPy and MWCNTs, Appl. Catal. B 258 (2019), 117969, https://doi.org/10.1016/j.apcatb.2019.117969.

[14] S. Chen, D. Huang, G. Zeng, W. Xue, L. Lei, P. Xu, R. Deng, J. Li, M. Cheng, In-situ synthesis of facet-dependent $BiVO_4$/Ag_3PO_4/PANI photocatalyst with enhanced visible-light-induced photocatalytic degradation performance: synergism of interfacial coupling and hole-transfer, Chem. Eng. J. 382 (2020), 122840, https://doi.org/10.1016/j.cej.2019.122840.

[15] Y. Lin, S. Wu, C. Yang, M. Chen, X. Li, Preparation of size-controlled silver phosphate catalysts and their enhanced photocatalysis performance via synergetic effect with MWCNTs and PANI, Appl. Catal. B 245 (2019) 71–86, https://doi.org/10.1016/j.apcatb.2018.12.048.

[16] Q. Xiang, D. Lang, T. Shen, F. Liu, Graphene-modified nanosized Ag_3PO_4 photocatalysts for enhanced visible-light photocatalytic activity and stability, Appl. Catal. B 162 (2015) 196–203, https://doi.org/10.1016/j.apcatb.2014.06.051.

[17] M. Rehan, A. Barhoum, T.A. Khattab, L. Gätjen, R. Wilken, Colored, photocatalytic, antimicrobial and UV-protected viscose fibers decorated with Ag/Ag_2CO_3 and Ag/Ag_3PO_4 nanoparticles, Cellul. 26 (9) (2019) 5437–5453, https://doi.org/10.1007/s10570-019-02497-8.

[18] X. Miao, X. Yue, Z. Ji, X. Shen, H. Zhou, M. Liu, K. Xu, J. Zhu, G. Zhu, L. Kong, S. A. Shah, Nitrogen-doped carbon dots decorated on g-C_3N_4/Ag_3PO_4 photocatalyst with improved visible light photocatalytic activity and mechanism insight, Appl. Catal. B 227 (2018) 459–469, https://doi.org/10.1016/j.apcatb.2018.01.057.

[19] T. Cai, W. Zeng, Y. Liu, L. Wang, W. Dong, H. Chen, X. Xia, A promising inorganic-organic Z-scheme photocatalyst Ag_3PO_4/PDI supermolecule with enhanced photoactivity and photostability for environmental remediation, Appl. Catal. B 263 (2020), 118327, https://doi.org/10.1016/j.apcatb.2019.118327.

[20] Y. He, L. Zhang, B. Teng, M. Fan, New application of Z-scheme Ag_3PO_4/g-C_3N_4 composite in converting CO_2 to fuel, Environ. Sci. Tech. 49 (1) (2015) 649–656, https://doi.org/10.1021/es5046309.

[21] T. Cai, L. Wang, Y. Liu, S. Zhang, W. Dong, H. Chen, X. Yi, J. Yuan, X. Xia, C. Liu, S. Luo, Ag_3PO_4/Ti_3C_2 MXene interface materials as a Schottky catalyst with enhanced photocatalytic activities and anti-photocorrosion performance, Appl. Catal. B 239 (2018) 545–554, https://doi.org/10.1016/j.apcatb.2018.08.053.

[22] Y. Lin, S. Wu, X. Li, X. Wu, C. Yang, G. Zeng, Y. Peng, Q. Zhou, L. Lu, Microstructure and performance of Z-scheme photocatalyst of silver phosphate modified by MWCNTs and Cr-doped $SrTiO_3$ for malachite green degradation, Appl. Catal. B 227 (2018) 557–570, https://doi.org/10.1016/j.apcatb.2018.01.054.

[23] Q. Xu, L. Zhang, B. Cheng, J. Fan, J. Yu, S-scheme heterojunction photocatalyst, Chem 6 (7) (2020) 1543–1559, https://doi.org/10.1016/j.chempr.2020.06.010.

[24] L. Zhang, J. Zhang, H. Yu, J. Yu, Emerging S-scheme photocatalyst, Adv. Mater. 34 (11) (2022), e2107668, https://doi.org/10.1002/adma.202107668.

[25] Q. Wang, Q. Gao, A.M. Al-Enizi, A. Nafady, S. Ma, Recent advances in MOF-based photocatalysis: environmental remediation under visible light, Inorg. Chem. Front. 7 (2) (2020) 300–339, https://doi.org/10.1039/c9qi01120j.

[26] Q. Wang, D. Astruc, State of the art and prospects in metal-organic framework (MOF)-based and MOF-derived nanocatalysis, Chem. Rev. 120 (2) (2020) 1438–1511, https://doi.org/10.1021/acs.chemrev.9b00223.

[27] G. Cai, P. Yan, L. Zhang, H.C. Zhou, H.L. Jiang, Metal-organic framework-based hierarchically porous materials: synthesis and applications, Chem. Rev. 121 (20) (2021) 12278–12326, https://doi.org/10.1021/acs.chemrev.1c00243.

[28] T. Wu, X. Liu, Y. Liu, M. Cheng, Z. Liu, G. Zeng, B. Shao, Q. Liang, W. Zhang, Q. He, W. Zhang, Application of QD-MOF composites for photocatalysis: energy production and environmental remediation, Coord. Chem. Rev. 403 (2020), 213097, https://doi.org/10.1016/j.ccr.2019.213097.

[29] X. Fang, Q. Shang, Y. Wang, L. Jiao, T. Yao, Y. Li, Q. Zhang, Y. Luo, H.L. Jiang, Single Pt atoms confined into a metal-organic framework for efficient photocatalysis, Adv. Mater. 30 (7) (2018), https://doi.org/10.1002/adma.201705112.

[30] K. Yu, I. Ahmed, D.I. Won, W.I. Lee, W.S. Ahn, Highly efficient adsorptive removal of sulfamethoxazole from aqueous solutions by porphyrinic MOF-525 and MOF-545, Chemosphere 250 (2020), 126133, https://doi.org/10.1016/j.chemosphere.2020.126133.

[31] H.Q. Xu, J. Hu, D. Wang, Z. Li, Q. Zhang, Y. Luo, S.H. Yu, H.L. Jiang, Visible-light photoreduction of CO_2 in a metal-organic framework: boosting electron-hole separation via electron trap states, J. Am. Chem. Soc. 137 (42) (2015) 13440–13443, https://doi.org/10.1021/jacs.5b08773.

[32] M.M. Baig, S. Zulfiqar, M.A. Yousuf, I. Shakir, M.F.A. Aboud, M.F. Warsi, $Dy_xMnFe_{2-x}O_4$ nanoparticles decorated over mesoporous silica for environmental remediation applications, J. Hazard. Mater. 402 (2021), 123526, https://doi.org/10.1016/j.jhazmat.2020.123526.

[33] H. Zhu, R. Jiang, J. Li, Y. Fu, S. Jiang, J. Yao, Magnetically recyclable Fe_3O_4/Bi_2S_3 microspheres for effective removal of Congo red dye by simultaneous adsorption and photocatalytic regeneration, Sep. Purif. Technol. 179 (2017) 184–193, https://doi.org/10.1016/j.seppur.2016.12.051.

[34] S. Li, M. Zhang, Z. Qu, X. Cui, Z. Liu, C. Piao, S. Li, J. Wang, Y. Song, Fabrication of highly active Z-scheme Ag/g-C_3N_4-Ag-Ag_3PO_4 (1 1 0) photocatalyst photocatalyst for visible light photocatalytic degradation of levofloxacin with simultaneous hydrogen production, Chem. Eng. J. 382 (2020), 122394, https://doi.org/10.1016/j.cej.2019.122394.

[35] D. Feng, Z.Y. Gu, J.R. Li, H.L. Jiang, Z. Wei, H.C. Zhou, Zirconium-metalloporphyrin PCN-222: mesoporous metal-organic frameworks with ultrahigh stability as biomimetic catalysts, Angew. Chem. Int. Ed. 51 (41) (2012) 10307–10310, https://doi.org/10.1002/anie.201204475.

[36] Y. Guo, X. Zhang, N. Xie, R. Guo, Y. Wang, Z. Sun, H. Li, H. Jia, D. Niu, H.B. Sun, Investigation of antimony adsorption on a zirconium-porphyrin-based metal-organic framework, Dalton Trans. 50 (39) (2021) 13932–13942, https://doi.org/10.1039/d1dt01895g.

[37] Y. Lin, H. Liu, C. Yang, X. Wu, C. Du, L. Jiang, Y. Zhong, Gama-graphyne as photogenerated electrons transfer layer enhances photocatalytic performance of silver phosphate, Appl. Catal. B 264 (2020), 118479, https://doi.org/10.1016/j.apcatb.2019.118479.

[38] Y. Lin, C. Yang, S. Wu, X. Li, Y. Chen, W.L. Yang, Construction of built-in electric field within silver phosphate photocatalyst for enhanced removal of recalcitrant organic pollutants, Adv. Funct. Mater. 30 (38) (2020) 2002918, https://doi.org/10.1002/adfm.202002918.

[39] Y. Lin, C. Yang, Q. Niu, S. Luo, Interfacial charge transfer between silver phosphate and W_2N_3 induced by nitrogen vacancies enhances removal of β-lactam antibiotics, Adv. Funct. Mater. 32 (5) (2021) 2108814, https://doi.org/10.1002/adfm.202108814.

[40] X. Li, P. Xu, M. Chen, G. Zeng, D. Wang, F. Chen, W. Tang, C. Chen, C. Zhang, X. Tan, Application of silver phosphate-based photocatalysts: barriers and solutions, Chem. Eng. J. 366 (2019) 339–357, https://doi.org/10.1016/j.cej.2019.02.083.

[41] W. Wu, C. Lu, M. Yuan, Y. Tian, H. Zhou, Acidification of potassium bismuthate for enhanced visible-light photocatalytic degradation ability: an effective strategy for regulating the abilities of adsorption, oxidation, and photocatalysis, Appl. Surf. Sci. 544 (2021), 148873, https://doi.org/10.1016/j.apsusc.2020.148873.

[42] F. Wang, Y. Wu, Y. Wang, J. Li, X. Jin, Q. Zhang, R. Li, S. Yan, H. Liu, Y. Feng, G. Liu, W. Lv, Construction of novel Z-scheme nitrogen-doped carbon dots/{0 0 1} TiO_2 nanosheet photocatalysts for broad-spectrum-driven diclofenac degradation: mechanism insight, products and effects of natural water matrices, Chem. Eng. J. 356 (2019) 857–868, https://doi.org/10.1016/j.cej.2018.09.092.

[43] L. Yan, J. Hou, T. Li, Y. Wang, C. Liu, T. Zhou, W. Jiang, D. Wang, G. Che, Tremella-like integrated carbon nitride with polyvinylimine-doped for enhancing photocatalytic degradation and hydrogen evolution performances, Sep. Purif. Technol. 279 (2021), 119766, https://doi.org/10.1016/j.seppur.2021.119766.

[44] Z. Liu, C. Zhang, L. Liu, T. Zhang, J. Wang, R. Wang, T. Du, C. Yang, L. Zhang, L. Xie, W. Zhu, T. Yue, J. Wang, A Conductive network and dipole field for harnessing photogenerated charge kinetics, Advanced Materials 33(48) (2021) e2104099. https://doi.org/10.1002/adma.202104099.

[45] Y. Yang, G. Zeng, D. Huang, C. Zhang, D. He, C. Zhou, W. Wang, W. Xiong, B. Song, H. Yi, S. Ye, X. Ren, In situ grown single-atom cobalt on polymeric carbon nitride with bidentate ligand for efficient photocatalytic degradation of refractory antibiotics, Small 16 (29) (2020) e2001634, doi:10.1002/smll.202001634.

[46] S. Zhang, S. Zhao, S. Huang, B. Hu, M. Wang, Z. Zhang, L. He, M. Du, Photocatalytic degradation of oxytetracycline under visible light by nanohybrids of CoFe alloy nanoparticles and nitrogen-/sulfur-codoped mesoporous carbon, Chem. Eng. J. 420 (2021), 130516, https://doi.org/10.1016/j.cej.2021.130516.

[47] R. Hassandoost, S.R. Pouran, A. Khataee, Y. Orooji, S.W. Joo, Hierarchically structured ternary heterojunctions based on Ce^{3+}/Ce^{4+} modified Fe_3O_4 nanoparticles anchored onto graphene oxide sheets as magnetic visible-light-active photocatalysts for decontamination of oxytetracycline, J. Hazard. Mater. 376 (2019) 200–211, https://doi.org/10.1016/j.jhazmat.2019.05.035.

[48] H. Guo, C.-G. Niu, C.-Y. Feng, C. Liang, L. Zhang, X.-J. Wen, Y. Yang, H.-Y. Liu, L. Li, L.-S. Lin, Steering exciton dissociation and charge migration in green synthetic oxygen-substituted ultrathin porous graphitic carbon nitride for boosted photocatalytic reactive oxygen species generation, Chem. Eng. J. 385 (2020), 123919, https://doi.org/10.1016/j.cej.2019.123919.

[49] M. Zhang, C. Lai, B. Li, F. Xu, D. Huang, S. Liu, L. Qin, Y. Fu, X. Liu, H. Yi, Y. Zhang, J. He, L. Chen, Unravelling the role of dual quantum dots cocatalyst in 0D/2D heterojunction photocatalyst for promoting photocatalytic organic pollutant degradation, Chem. Eng. J. 396 (2020), 125343, https://doi.org/10.1016/j.cej.2020.125343.

[50] Y. Li, Z. Lai, Z. Huang, H. Wang, C. Zhao, G. Ruan, F. Du, Fabrication of BiOBr/MoS_2/graphene oxide composites for efficient adsorption and photocatalytic removal of tetracycline antibiotics, Appl. Surf. Sci. 550 (2021), 149342, https://doi.org/10.1016/j.apsusc.2021.149342.

[51] H. Sun, T. Zhou, J. Kang, Y. Zhao, Y. Zhang, T. Wang, X. Yin, High-efficient degradation of oxytetracycline by visible photo-Fenton process using $MnFe_2O_4$/g-C_3N_4: performance and mechanisms, Sep. Purif. Technol. 299 (2022), 121771, https://doi.org/10.1016/j.seppur.2022.121771.

[52] K. Ouyang, C. Yang, B. Xu, H. Wang, S. Xie, Synthesis of novel ternary Ag/$BiVO_4$/GO photocatalyst for degradation of oxytetracycline hydrochloride under visible light, Colloids Surf A Physicochem Eng Asp 625 (2021), 126978, https://doi.org/10.1016/j.colsurfa.2021.126978.

[53] L. Yi, J. Qin, H. Sun, Y. Ruan, D. Fang, J. Wang, Construction of Z-scheme (TiO_2/Er^{3+}:$YAlO_3$)/$NiFe_2O_4$ photocatalyst composite for intensifying hydrodynamic cavitation degradation of oxytetracycline in aqueous solution, Sep. Purif. Technol. 293 (2022), 121138, https://doi.org/10.1016/j.seppur.2022.121138.

[54] X. Liu, Y. Pei, M. Cao, H. Yang, Y. Li, Highly dispersed copper single-atom catalysts activated peroxymonosulfate for oxytetracycline removal from water: mechanism and degradation pathway, Chem. Eng. J. 450 (2022), 138194, https://doi.org/10.1016/j.cej.2022.138194.

[55] D. Liu, M. Li, X. Li, F. Ren, P. Sun, L. Zhou, Core-shell Zn/Co MOFs derived Co_3O_4/CNTs as an efficient magnetic heterogeneous catalyst for persulfate activation and oxytetracycline degradation, Chem. Eng. J. 387 (2020), 124008, https://doi.org/10.1016/j.cej.2019.124008.

[56] Y. Wang, L. Ding, C. Liu, Y. Lu, Q. Wu, C. Wang, Q. Hu, 0D/2D/2D $ZnFe_2O_4$/$Bi_2O_2CO_3$/BiOBr double Z-scheme heterojunctions for the removal of tetracycline antibiotics by permonosulfate activation: photocatalytic and non-photocatalytic mechanisms, radical and non-radical pathways, Sep. Purif. Technol. 283 (2022), 120164, https://doi.org/10.1016/j.seppur.2021.120164.

[57] G. Li, Z. Lian, Z. Wan, Z. Liu, J. Qian, Y. Deng, S. Zhang, Q. Zhong, Efficient photothermal-assisted photocatalytic NO removal on molecular cobalt phthalocyanine/Bi_2WO_6 Z-scheme heterojunctions by promoting charge transfer and oxygen activation, Appl. Catal. B 317 (2022), 121787, https://doi.org/10.1016/j.apcatb.2022.121787.

[58] P. Xia, S. Cao, B. Zhu, M. Liu, M. Shi, J. Yu, Y. Zhang, Designing a 0D/2D S-scheme heterojunction over polymeric carbon nitride for visible-light photocatalytic inactivation of bacteria, Angew. Chem. Int. Ed. 59 (13) (2020) 5218–5225, https://doi.org/10.1002/anie.201916012.

[59] W. Zhao, Y. Feng, H. Huang, P. Zhou, J. Li, L. Zhang, B. Dai, J. Xu, F. Zhu, N. Sheng, D.Y.C. Leung, A novel Z-scheme Ag_3VO_4/$BiVO_4$ heterojunction photocatalyst: study on the excellent photocatalytic performance and photocatalytic mechanism, Appl. Catal. B 245 (2019) 448–458, https://doi.org/10.1016/j.apcatb.2019.01.001.

[60] S. Chen, D. Huang, G. Zeng, X. Gong, W. Xue, J. Li, Y. Yang, C. Zhou, Z. Li, X. Yan, T. Li, Q. Zhang, Modifying delafossite silver ferrite with polyaniline: Visible-light-response Z-scheme heterojunction with charge transfer driven by internal electric field, Chem. Eng. J. 370 (2019) 1087–1100, https://doi.org/10.1016/j.cej.2019.03.282.

[61] F. Xu, K. Meng, B. Cheng, S. Wang, J. Xu, J. Yu, Unique S-scheme heterojunctions in self-assembled TiO_2/$CsPbBr_3$ hybrids for CO_2 photoreduction, Nat. Commun. 11 (1) (2020) 4613, https://doi.org/10.1038/s41467-020-18350-7.